Short- and intermediate-range order in MCl_2 melts: the importance of anionic polarization

1993 J. Phys.: Condens. Matter 5 6833

(http://iopscience.iop.org/0953-8984/5/37/004)

J. Phys.: Condens. Matter 5 (1993) 6833–6844. Printed in the UK

Short- and intermediate-range order in MCl_2 melts: the importance of anionic polarization

M Wilson and P A Madden

Physical Chemistry Laboratory, Oxford University, South Parks Road, Oxford OX1 3QZ, UK

Received 20 May 1993, in final form 12 July 1993

Abstract. The partial radial distribution functions $g_{\alpha\beta}(r)$ and partial structure factors $S_{\alpha\beta}(k)$ obtained in computer simulations of the ionic melts of stoichiometry MCl_2 with a recently introduced polarizable ion model are described. The calculated quantities exhibit distinctive structural features which have been discovered experimentally and attributed to 'covalency'. These include a shift in the position of the principal peak of $g_{++}(r)$ relative to $g_{--}(r)$ with decreasing cation size and a pre-peak in $S_{++}(k)$.

1. Introduction

Extensive neutron scattering studies of the molten halides of alkaline earth and other metals with doubly charged ions have revealed an intriguing evolution of the short-range order with cation size [1–5]. Partial radial distribution functions (RDFs) for the different ionic species g_{++}, g_{--} and g_{+-} have been separated by the isotopic substitution method [6]. The most extensive data are for the chlorides, on which we will focus, but the more limited data available for other halides appear to fit into the pattern we outline below.

For large cations, exemplified by $BaCl_2$ [7] as shown in figure 1(*a*), the liquid RDFs can be readily interpreted from their resemblance to those of the fluorite structure (into which $BaCl_2$ and $SrCl_2$ crystallize). In the perfect fluorite structure the anions form a simple cubic lattice with the cations occupying the centres of alternate cubes, which are corner sharing, giving an overall FCC arrangement ($Fm3m$). The RDFs for the solid therefore show a nearest-neighbour peak in g_{+-} (at half the cube diagonal) which integrates to a coordination number, n_{+-}, of eight. The next-nearest-neighbour peak is in g_{--}, at the cube edge separation: the first peak in g_{++} appears at still larger separations—the full cube diagonal. A simplistic view of the fluorite structure is that it is optimal for maximizing the distance between the highly charged cations for radius ratios in the range $1 \leqslant \sigma_-/\sigma_+ \leqslant 1.37$. These fluorite features are clearly preserved in the $BaCl_2$ melt RDFs shown in the figure, and n_{+-}, determined by integrating to the first minimum in g_{+-}, is 7.7 [7].

As cation size diminishes (a set of crystal radii is given in table 1 for guidance) the melt RDFs depart more and more strongly from this simple ionic picture although the out-of-phase oscillations of the unlike and like partial RDFs indicate the continued importance of coulombic effects. On moving to Ca, Mg and Zn the first peak in g_{+-} sharpens and n_{+-} diminishes to a value of approximately 4 (see table 1), which *suggests* local tetrahedral coordination. There is also a marked inward shift of the first peak in g_{++} relative to that in g_{--}. This trend is already apparent for $SrCl_2$ (figure 1(b)), but is pronounced for $MgCl_2$ (1(c)) and $ZnCl_2$ (1(d)) where the first peaks of g_{++} and g_{--} coincide, contrary to the requirement of maximizing the separation of highly charged cations. Computer simulations

0953-8984/93/376833+12$07.50

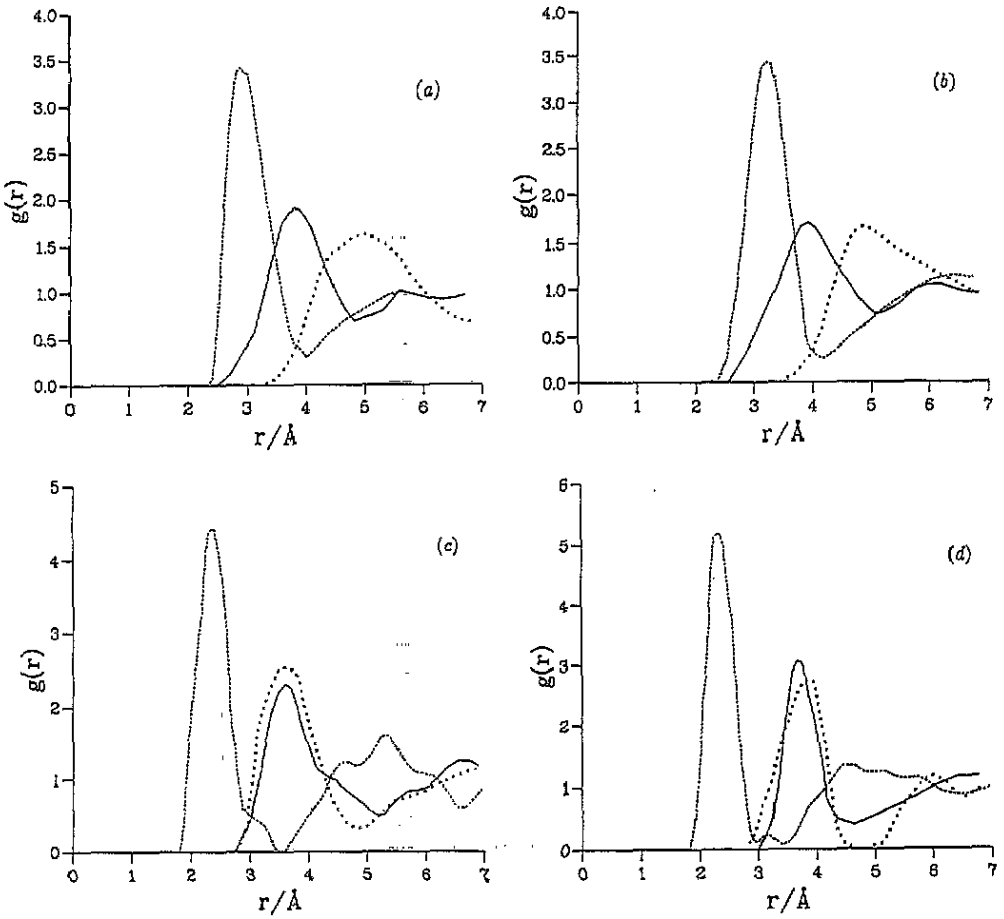

Figure 1. The experimental partial RDFs g_{++} (dots), g_{--} (solid line) and g_{+-} (dashed) for (*a*) $BaCl_2$ [7], (*b*)$SrCl_2$ [8], (*c*) $MgCl_2$ [9] and (*d*) $ZnCl_2$ [10].

Table 1. Experimental cation radii and coordination numbers for the divalent cation halides under investigation.

Cation	σ_+ (au)	Coordination number
Mg^{2+}	1.228	4.3
Zn^{2+}	1.398	4.3
Ni^{2+}	1.474	4.7
Ca^{2+}	1.871	5.4
Sr^{2+}	2.135	6.6
Ba^{2+}	2.551	7.7

based upon a 'rigid-ion' model, with Born–Mayer pair potentials, cannot reproduce this behaviour [11, 12]—a fluorite-like ordering of the peaks in g_{++} and g_{--} appears unless unphysically large dispersion interactions between the cations are introduced [13]. Coupled with the change in melt RDFs with diminishing cation size, there is also a change in the structure of the crystals into which these materials crystallize. $CaCl_2$ forms a distorted rutile structure (*Pnnm*) [14] whereas $MgCl_2$ forms the layered CdI_2 structure, in which adjacent

hexagonal layers of anions alternate with layers of metal ions ($C\bar{3}m$). Whilst the general change from the eight-coordinated fluorite structure to six-coordinated structures can be predicted through radius-ratio rules (i.e. it is a packing effect) the relationships between the six-coordinated structures are more difficult to understand [15].

The RDF data we have surveyed focuses attention on the short-range order in the melts, i.e. on the integrated intensity of the first peaks and their relative positions. The scattering data have shown another unexplained structural characteristic of the chloride melts with intermediate sized cations (Ca, Mg, Zn), which is related to the order at longer range. In the cation–cation partial structure factor $S_{++}(k)$ of these systems there appears a 'pre-peak' at momentum transfers $k = k_p$ which are about half the principal peak values (i.e. at around 1 $Å^{-1}$); crudely speaking, then, the pre-peak is associated with structure on a length scale about twice the shortest cation–cation separations in the melt and is thus regarded as the signature of 'intermediate-range order' in the melt. Wood and Howe *et al* [4] have noted the similarity between k_p and the Bragg peaks related to the correlation between the planes of cations in systems that crystallize in the CdI_2 structure. The phenomenon is not a pre-crystallization effect, however, as the amplitude of the pre-peak does not diminish with increasing temperature, at least in $ZnCl_2$ [16]. Furthermore, not all systems that exhibit a pre-peak in the melt crystallize into a layered structure.

To summarize, then, as the cation size diminishes the MX_2 melts develop local and intermediate-range order which is not readily explained on a simple ionic model. This, coupled with the fact that these systems form crystals which contain such non-coulombic features as adjacent layers of anions (CdI_2 structure), has lead to the suggestion that these structures are a consequence of 'covalent' interactions. Enderby and Barnes [2] describe covalency as 'interactions which change the charge distribution of the valence electrons ...' and have stressed the crucial role of the size of the cation, rather than its specific electronic configuration, in determining the structure in the melt. Chemists would probably prefer a less catholic description of covalency which implied charge redistribution *between* anion and cation. It is our purpose in this paper to show that all the data on MX_2 melts which we have surveyed can be explained without invoking charge transfer and within the ionic model *provided that the effects of ionic polarization (induction forces) are included.* Elsewhere [15] we will discuss the preferred crystal structures from the same viewpoint. Our objective is to show that a simple potential, based upon the ionic model, with no change in parameters save the cation radius, can encompass the range of behaviour we have detailed. Our concern is to identify the simplest model that accounts for the trends, rather than account in detail for specific systems.

2. The model

The way in which the ion polarizability is included in our simulations was described in detail in an earlier paper [17]. Briefly, dipoles induced in the polarizable ions are represented by rods of fixed length but variable orientation with variable charges on the ends. The rod orientation and the dynamic charges are determined self-consistently from the total coulomb field acting on each ion, which arises from the charges and induced dipoles on the other ions in the system. In addition, short-range ('induction-damping') potentials may be included, which represent the way the induced dipole between a pair of ions differs from the pure Coulomb value when their charge distributions overlap. The instantaneous induced dipoles in the simulation are determined by an application of the Car–Parrinello method [18, 19]; similar techniques were introduced by Sprik *et al* [20–23] to represent the induced dipoles

in water. Since the full self-consistent induced dipoles are used in the calculation of the interionic forces the non-additivity of the induction effects is included. The treatment of the dipole polarizability is similar in spirit to that in the shell model [24], except that all the parameters in our model have a well defined microscopic significance and may be determined *a priori* from electronic structure calculations. Systematic application of the shell model to the melts of interest here has been precluded by difficulties in parametrizing the model and by technical difficulties such as energy conservation. A recent paper suggests that these technical problems may now be solved [25].

Besides the induction effects, we include the short-range, overlap-repulsion and dispersion interactions between the ions by including a pair potential of Born–Mayer form between the ions, i.e.

$$u(r_{ij}) = B_{ij}\exp(-a_{ij}r_{ij}) - C_{ij}/r_{ij}^6 - D_{ij}/r_{ij}^8 + Q_iQ_j/r_{ij} \tag{2.1}$$

where the parameters B_{ij}, a_{ij}, C_{ij} and D_{ij} have their usual meaning [24]. Note that adding induction effects to the Born–Mayer potentials is not inconsistent as the pair induction terms, which would be proportional to r_{ij}^{-4}, are explicitly *excluded* from the Born–Mayer form since in cubic crystals the pair charge-induced dipole is completely cancelled by a three-body term due to the high symmetry. In the melt (and crystals of lower symmetry) these terms survive and, as we will show, play an important role.

2.1. *Parameters of the model*

We will describe the results from a series of simulations with potentials which differ only in the choice of cation radius. For the present, we will neglect induction damping. In order to focus on the subtle structural effects which arise from the interplay of the induced dipoles on the anions and short-range forces we neglect any contributions to the potential that do not influence the structure (as opposed to the energy). For this reason we omit *all* dispersion terms (we have shown that physically reasonable choices for the dispersion terms [26] do not radically change the structures) and also neglect the cation–cation Born–Mayer repulsion, since Coulomb repulsion is sufficient to keep the cations apart. We further neglect the role of induced dipoles on the cations; we can anticipate that these will be less important than those on the anions. The induction energy of the cation charge with the anion polarizability is proportional to $Q_+^2\alpha_-$, compared with $Q_-^2\alpha_+$ for the anion charge with the cation polarizability. Even for the most polarizable cation Ba^{2+}, α_+ is only half the Cl^- polarizability [26], so that $Q_+^2\alpha_-$ is larger than $Q_-^2\alpha_+$ by a factor of eight.

We choose the remaining parameters in the spirit of a strict ionic model, in which formal charges are used for Q_+ and Q_- and in which the anion properties are kept constant, irrespective of the particular cation; in reality, of course, some variation is expected [26,27]. The Cl^- polarizability, which fully determines the induced dipoles, is chosen to be 20 au—essentially the value for Cl^- in an NaCl crystal [27]. The short-range anion–anion interaction parameters B_{--} and a_{--} are fixed at $B_{--} = 25.00$ and $a_{--} = 1.3$. These give a similar potential energy curve to the values utilized by de Leeuw [28,29] from fits of the properties of the $SrCl_2$ crystal by Busing [30] ($B_{--} = 20.61$ and $a_{--} = 1.11$).

The remaining parameters B_{+-} and a_{+-} determine the repulsion between the cation and anion. The parameter a_{+-}, that controls the steepness of the repulsion, is fixed at 1.6 au—the value used by de Leeuw for $SrCl_2$. This parameter is determined by the rate of change of overlap of the tails of the charge densities of the cation and anion which should be almost independent of the specific cation. The cation density can be expected to drop very steeply with distance from the cation centre so that the value of a_{+-} should be

determined by the shape of the relatively diffuse charge density around the Cl^- ion. B_{+-} is the only parameter in our model that depends on the identity of the cation, it controls the amplitude of the repulsion at a given separation. As such, it can be regarded as a measure of the cation radius σ_+ since we may rewrite the Born–Mayer repulsion in the form

$$B_{+-}\exp(-a_{+-}r_{ij}) = A\exp\{-a_{+-}[r_{ij} - (\sigma_+ + \sigma_-)]\} \tag{2.2}$$

and, in the spirit of the rest of the model, regard the Cl^- radius σ_- and A as constants. Table 1 gives the experimental cation radii whilst table 2 gives those derived from our B_{+-} term fixing the B_{+-} = 150 au term as giving the cation radius of Ba^{2+}. We see that this means that the other cation radii are consistently higher than the crystal radii of table 1. This is consistent with the model as we are neglecting short-ranged induced dipoles (or induction damping) and hence the anions require a larger effective cation radius to prevent them from overpolarizing [17].

Table 2. Effective cation radii and coordination numbers for the generalized MCl_2 model.

B_{+-} (au)	σ_+ (au)	Coordination number
60	1.98	2.06
65	2.03	3.76
70	2.07	4.22
80	2.16	4.58
100	2.30	5.45
120	2.41	6.20
135	2.49	6.42
150	2.55	6.63

The simulation system consists of 108 MCl_2 'molecules' (i.e. 324 ions). The same number density was used in all the simulations, irrespective of the effective cation radius. The box length was fixed at 42 au, which gives the melting density for $SrCl_2$. Again, this is done in the spirit of using the simplest model possible to look at the trends although, somewhat surprisingly, the actual experimental densities for the melts of the smaller cations do not differ substantially from this value. All simulations were performed at a temperature of 1200 K, roughly the melting temperature of $SrCl_2$. The experimental temperatures for some of the melts (notably $ZnCl_2$) are significantly lower. Each run was over 10 000 steps with a timestep of 20 au (=0.5×10^{-15} s).

3. Simulation results

3.1. Short-range order

Figure 2 shows the results obtained with the polarizable ion model (PIM) for four values of B_{+-}. The evolution of the RDFs with decreasing cation radius (decreasing B_{+-}) parallels that found experimentally in the series Ba^{2+} (similar to B_{+-} =150 au), Sr^{2+} (B_{+-} = 120 au), and Mg^{2+}/Zn^{2+} (B_{+-} =100 au). The inward shift of the g_{++} peak and the increased sharpness and decreasing coordination number (see table 1) of g_{+-} are reproduced. Comparison of the ionic crystal radii in table 1 with the effective cation radii, obtained from equation (2.2), given in table 2 shows that this agreement is reached for physically reasonable values of the short-range repulsion parameters. The shapes of g_{++} and g_{--}, especially for Mg^{2+}/Zn^{2+},

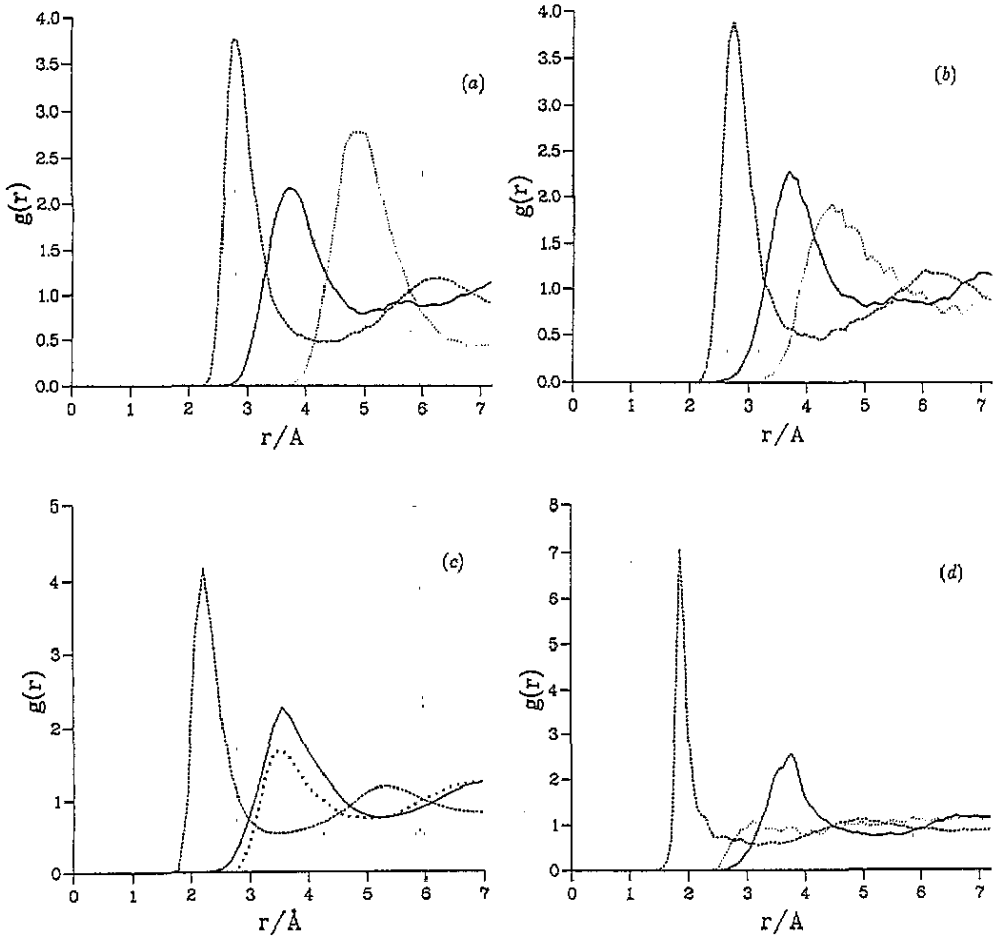

Figure 2. Partial RDFs for the PIM for different values of the short-range repulsion parameter B_{+-} (effective cation radius): (*a*) B_{+-} = 150 au, compare figure 1(*a*); (*b*) B_{+-} = 120 au, compare figure 1(b); (*c*) B_{+-} = 100 au; (*d*) B_{+-} = 60 au

are not in good accord with the experimental ones; a good deal of improvement would be brought about simply by carrying out the simulations at the experimental temperatures, but to obtain detailed agreement the very simple potentials we have used would need refinement—as we have said in section 1, this is not our goal here.

Figure 2(*d*) shows the RDFs in the extreme of small cation radius (B_{+-} = 60 au); there seems to be no experimentally studied chloride to which these data pertain. However, the extremely sharp peak in g_{+-} and the almost structureless forms of g_{++} and g_{--} are reminiscent of the observations on NiI_2 [31].

In figure 3 we contrast the RDFs for the PIM with those obtained for rigid-ion models (RIMs), which are identical in every way to those in the PIM except that the anion polarizability is set to zero. In agreement with previous RIM simulations [11, 12], we find that the fluorite-like ordering of the first peaks in g_{++} and g_{--} is preserved, irrespective of the cation radius. This comparison indicates that the major features of the evolution of short-range structure with cation radius observed experimentally are attributable to the induction forces caused by anionic polarization and their interplay with packing effects.

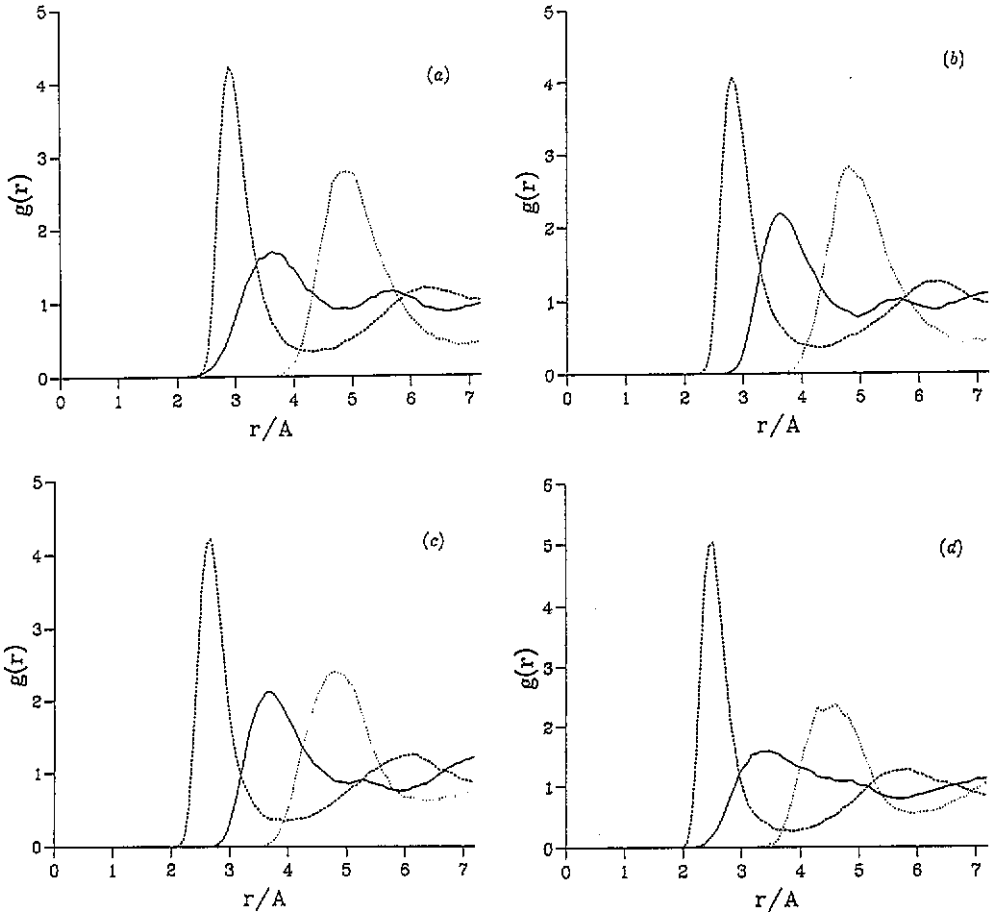

Figure 3. As figure 2 but for the RIM.

3.2. Intermediate-range order

As noted in section 1 a prominent pre-peak is observed experimentally in the cation–cation structure factor $S_{++}(k)$ for the smaller cations, and is indicative of intermediate-range order. The pre-peak is seen for $MgCl_2$, $ZnCl_2$, $CaCl_2$ and in the nickel halides but is absent for $BaCl_2$ and $SrCl_2$.

To compare the simulation results for $S_{++}(k)$ with experiment we must be careful to avoid introducing artifacts associated with the limited system size and the consequential truncation errors in Fourier transforms. Hence we obtain the structure factors directly, by calculating

$$S_{\alpha\beta}(k) = \frac{1}{\sqrt{N_\alpha N_\beta}} \left\langle \sum_{i\in\alpha} \sum_{j\in\beta} \exp(i\boldsymbol{k}\cdot\boldsymbol{r}_{ij}) \right\rangle \tag{3.1}$$

rather than by Fourier transformation of the RDFs. The calculation is performed at those wavevectors $\boldsymbol{k}$ that are commensurate with the periodic boundary conditions used in the simulation; i.e. are of the form $\boldsymbol{k} = (2\pi/L)(m, n, p)$, where m, n, and p are integers and L is the cell length. $S_{\alpha\beta}(k)$ is then obtained by averaging over $\boldsymbol{k}$ vectors of equal length.

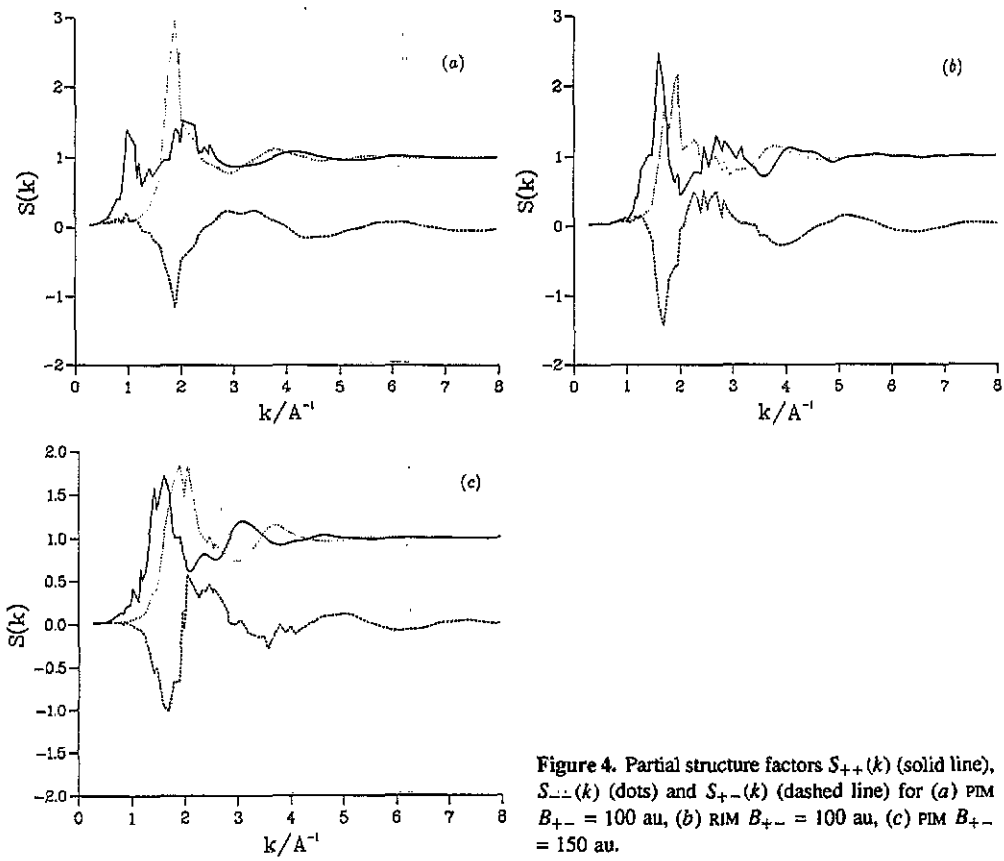

Figure 4. Partial structure factors $S_{++}(k)$ (solid line), $S_{--}(k)$ (dots) and $S_{+-}(k)$ (dashed line) for (*a*) PIM B_{+-} = 100 au, (*b*) RIM B_{+-} = 100 au, (*c*) PIM B_{+-} = 150 au.

In figure 4 we show the full set of partial structure factors calculated in the simulations. In figure 4(*a*) the results for B_{+-} = 100 au (Mg^{2+}/Zn^{2+}) in the PIM are shown. The partial structure factors resemble the experimental ones quite closely [9, 10]; the pre-peak in $S_{++}(k)$ is prominent. We have confirmed that the pre-peak is still present and unshifted in a much larger system containing 768 ions. The PIM data may be contrasted with those shown in figure 4(*b*), which is for the RIM at the same value of B_{+-} = 100 au—no pre-peak is visible. Finally in figure 4(*c*) we show the effect of increasing cation radius to the 'Ba^{2+}' value, B_{+-} = 150 au, in the PIM. No pre-peak is found, in agreement with the experimental findings. Hence, the pre-peak can be attributed directly to the effects introduced by the inclusion of induction terms.

4. Structural analysis

We have examined the instantaneous structures adopted by the ions in the course of the simulations using a molecular graphics package [32]. A typical configuration from the B_{+-} = 100 au run is shown in figure 5. The positions of the cations are indicated by the small dark spheres and those of the anions by the larger shaded spheres. The sizes of these spheres have been chosen to be only a small fraction of the actual ionic radii in order that the coordination structure of the melt can be clearly seen. In order to show this structure, ions whose separation is less than 6.8 au (i.e. the position of the first minimum in g_{+-} for

B_{+-} = 100 au) have been joined by a 'bond'. Note that we have not attempted to implement periodic boundary conditions in representing these bonds, so the ions at the edges of the cell are undercoordinated and not representative. In order to avoid cluttering the figure with too many ions, only the ions within a slice of width $\frac{1}{3}L$ are shown.

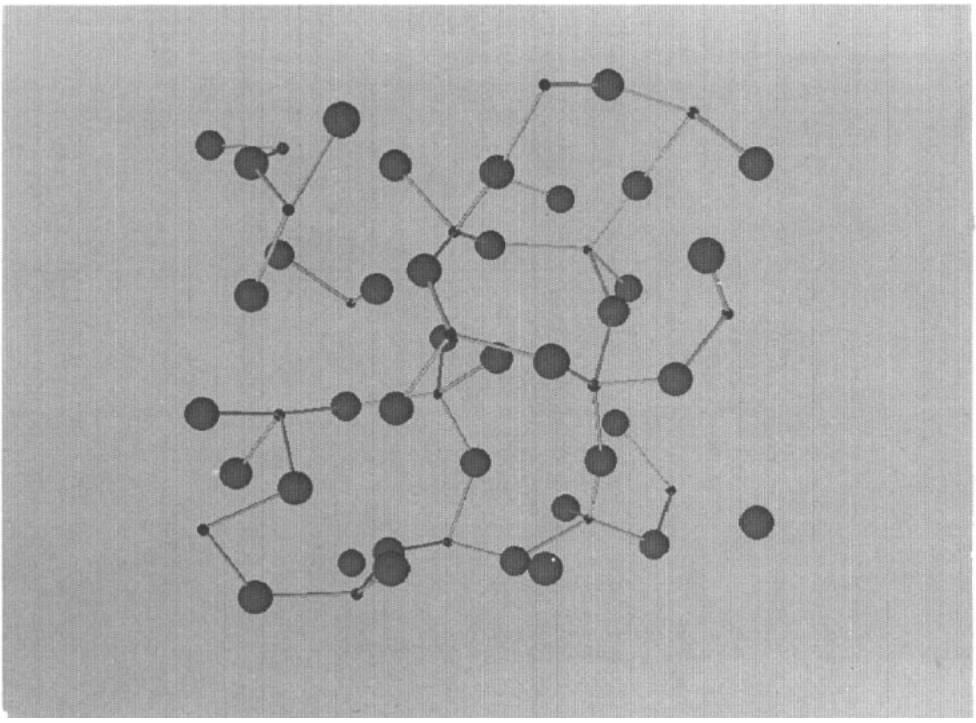

Figure 5. A snapshot of the B_{+-} = 100 au PIM run indicating the occurrence of a network of tetrahedral structures. The small dark spheres are cations and the large spheres are the anions. Bonds connect ions closer together than 6.8 au.

The local tetrahedral coordination around the cations is immediately evident from the figure. These tetrahedra form networks which extend across the simulation cell. Adjacent tetrahedra are connected at a common *corner*. It is this corner sharing attribute which is facilitated by the polarizable anions; we will see shortly why polarizability favours these structures. That the three-dimensional structure can be described as a network of corner-sharing tetrahedra allows us to see why why the first peaks in g_{++} and g_{--} coincide. A crystalline system with this local structure would be ZnS, consisting of interpenetrating FCC lattices, occupied by cations and anions respectively, and displaced by $(\frac{1}{4}, \frac{1}{4}, \frac{1}{4})$ (as in diamond). In this structure the nearest-neighbour cation–cation and anion–anion separations are equal. In the MX_2 system only half of the sites on the cation sublattice will be occupied but the particle separations will remain equal. The origin of the pre-peak observed in $S_{++}(k)$ for this system is not immediately obvious as a specific intermediate-range order in the real space structure. However, we can see that the network tends to form rings of intermediate size which could be associated with this phenomenon.

The reason why polarizable anions tend to form *non-linear* bridging sites between a pair of cations is that the dipole induced by the cations on the anion lies in the M–X–M plane in such a way as to effectively interpose a negative charge along the line of centres between the two cations. The cation–cation repulsive Coulomb interactions are therefore *screened* by the polarizable anions. This description has much in common with the mechanism suggested by Ballone *et al* [33] to account for the shortened cation–cation separation in the MX_2 systems.

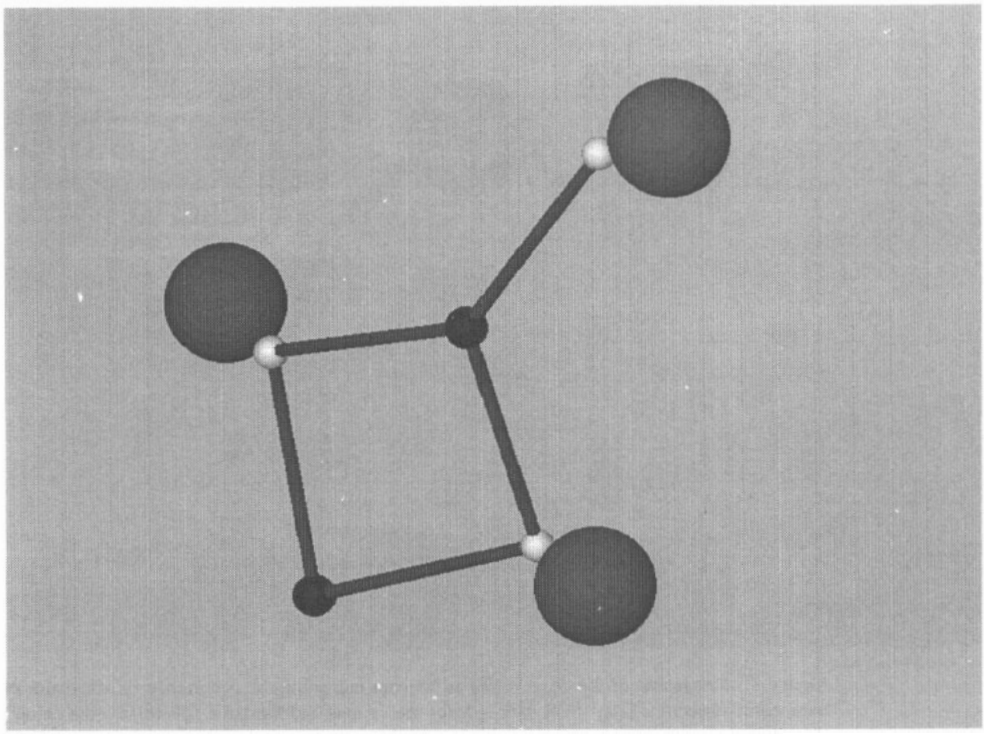

Figure 6. A close-up of an anion bridging structure in the B_{+-} = 80 au run. The negative end of the instantaneous dipole in each anion is indicated by a white sphere.

This mechanism can be clearly seen in figure 6 where we have explicitly indicated the negatively charged ends of the induced dipoles with small white spheres placed along the direction of the dipole vector at 1 au from the centre of the anion.

The comparison of figure 5 with the data obtained for the smaller cation in figure 6 allows us to illustrate the subtle interplay between induction and packing effects and the rich variety of structures which thereby emerge. At B_{+-} = 100 au the anion polarization favours single bridges between adjacent tetrahedra but for the smaller cations (B_{+-} = 80 au) double bridges tend to form between adjacent cations, this leads to local four-membered ring structures and a break-up of the tetrahedral network. An alternative viewpoint is that the corner-sharing tendency becomes an edge-sharing tendency as the cation size is reduced. The extreme situation of very small cations (B_{+-} = 60 au, the 'NiI_2' analogue of figure 6 is illustrated in figure 7; again the negative dipole ends are shown as white spheres). Here we see a quasimolecular MX_2 liquid in which the MX_2 'molecules' are non-linear.

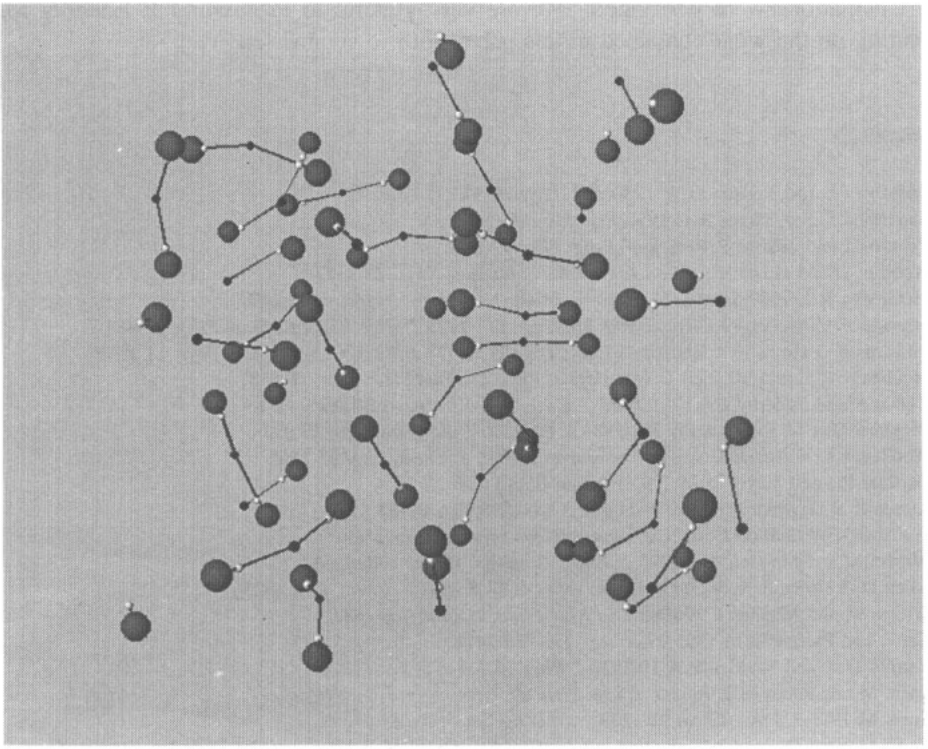

Figure 7. The quasimolecular structures that appear for large ratios of the anion to cation radius, at $B_{+-} = 60$ au.

5. Conclusion

We have shown that we can qualitatively account for the cation radius dependence of the experimental data on the short- and intermediate-range order in molten MCl_2 systems by allowing for the effects of anion polarization in the potential. The potential parameters take physically reasonable values and support a strictly ionic interpretation for the origin of the structure in these systems. We have deliberately used a very simple potential and changed only one parameter—the cation radius—in order stress the rich structural behaviour which arises solely from the interplay between induction and packing. Direct comparison with rigid ion simulations, lacking polarizable anions but otherwise identical, shows that the observed effects are directly attributable to the induction phenomenon. To obtain quantitative agreement between the calculated RDFs and experiment more refined potentials will be required to represent dispersion, induction damping and the dependence of the range of short-range repulsions on the identity of the cation.

Acknowledgments

MW would like to thank SERC and the Royal Signals and Radar Establishment (RSRE) Malvern for CASE award No 91565144. This work was sponsored by SERC through grant No GR/H10276, allowing the purchase of two IBM series 6000 320H machines on which

all the calculations were performed. We are very grateful to Professor J E Enderby for commenting on the work contained in this paper prior to submission.

References

[1] Enderby J E and Neilson G W 1980 *Adv. Phys* **29** 323
[2] Enderby J E and Barnes A C 1990 *Rep. Prog. Phys* **53** 85
[3] Rovere M and Tosi M P 1986 *Rep. Prog. Phys* **49** 1001
[4] Wood N D and Howe R A 1988 *J. Phys. C: Solid State Phys.* **21** 3177
[5] McGreevy R L 1987 *Solid State Physics* vol 40 (New York: Academic) p 247
[6] Edwards F G Enderby J E Howe R A and Page D I 1975 *J. Phys. C: Solid State Phys.* **8** 3483
[7] Edwards F G Howe R A Enderby J E and Page D I 1978 *J. Phys. C: Solid State Phys.* **11** 1053
[8] McGreevy R L and Mitchell E W J 1983 *J. Phys. C: Solid State Phys.* **15** 5537
[9] Biggin S and Enderby J E 1981 *J. Phys. C: Solid State Phys.* **14** 3129
[10] Biggin S Gay M and Enderby J E 1984 *J. Phys. C: Solid State Phys.* **17** 977
[11] Woodcock L V Angell C A and Cheeseman P 1976 *J. Chem. Phys* **65** 1565
[12] Gardner P J and Heyes D M 1985 *Physica* B **113** 227
[13] Kumta P N Deymier P A and Risbud S H 1988 *Physica* B **153** 85
[14] Wyckoff R W G 1965 *Crystal Structures* (New York: Interscience)
[15] Wilson M and Madden P A 1993 *J. Phys.: Condens. Matter* submitted
[16] Allen D A Howe R A, Wood N D and Howells W S 1991 *J. Chem. Phys* **94** 5071
[17] Wilson M and Madden P A 1993 *J. Phys.: Condens. Matter* **5** 2687
[18] Car R and Parrinello M 1985 *Phys. Rev. Lett.* **55** 2471
[19] Remler D K and Madden P A 1990 *Mol. Phys* **70** 921
[20] Sprik M and Klein M L 1988 *J. Chem. Phys* **89** 7556
[21] Sprik M 1991 *J. Phys. Chem* **95** 2283
[22] Sprik M 1993 *Computer Simulation in Chemical Physics* ed M P Allen and D J Tildesley (Berlin: Kluwer)
[23] Sprik M, Klein M L and Watanabe K 1990 *J. Phys. Chem* **94** 6483
[24] Sangster M J L and Dixon M 1976 *Adv. Phys* **23** 247
[25] Lindan P J D and Gillan M J 1993 *J. Phys: Condens. Matter* **5** 1019
[26] Pyper N C 1991 *Adv. Solid State Chem.* **2** 223
[27] Fowler P W and Madden P A 1984 *Phys. Rev.* B **29** 1035
[28] De Leeuw S W 1978 *Mol. Phys.* **36** 103
[29] De Leeuw S W 1978 *Mol. Phys.* **36** 765
[30] Busing R W 1970 *Trans. Am. Crystallogr. Assoc.* **6** 57
[31] Newport R J, Howe R A and Wood N D 1985 *J. Phys. C: Solid State Phys.* **18** 5249
[32] Advance Visualization Software Ltd. Licensed through the CHEST deal.
[33] Ballone P, Pastore G, Thakur J S and Tosi M P 1986 *Physica* B **142** 294